Complex multi-step martensitic twinning process during plastic deformation of the superelastic Ti-20Zr-3Mo-3Sn alloy

J. J. Gao, P. Castany, T. Gloriant

Complex multi-step martensitic twinning process during plastic deformation of the superelastic Ti-20Zr-3Mo-3Sn alloy

J.J. Gao, P. Castany*, T. Gloriant

Univ Rennes, INSA Rennes, CNRS, ISCR UMR 6226, 35000 Rennes, France

Abstract:

The Ti-20Zr-3Mo-3Sn (at.%) alloy is investigated before and after deformation by conventional and cyclic tensile tests, electron back-scattered diffraction (EBSD), *in situ* synchrotron X-ray diffraction (SXRD) and transmission electron microscopy (TEM). On one hand, the maximum recovery strain of 3.3% is obtained, which is attributed to the favorable $\{111\}<101>_{\beta}$ texture of β phase after short solution treatment. On the other hand, plastic deformation mechanisms are studied from specimens strained to 5% and 8%. The reversible stress-induced martensitic (SIM) α" transformation is preliminary detected by SXRD during loading and after unloading in both specimens. Then, the deformation microstructures are further investigated in details by TEM. At 5% of strain, primary α" deformation bands are observed with an abnormal orientation relationship (OR) with β phase. From crystallographic reconstruction, this OR is shown to be due to $\{130\}<310>_{\alpha''}$ twinning followed by $\{111\}_{\alpha''}$ type I reorientation twinning during loading. At 8% of strain, a complex hierarchical microstructure composed of primary and secondary α" bands is observed, which corresponds to residual primary $\{130\}<310>_{\alpha''}$ twins with secondary $\{130\}<310>_{\alpha''}$ twins occurring after $\{111\}_{\alpha''}$ reorientation twinning of primary $\{130\}<310>_{\alpha''}$ twins. The sequence of plastic deformation is then composed of primary $\{130\}<310>_{\alpha''}$ twinning, followed by $\{111\}_{\alpha''}$ reorientation twinning and finally secondary $\{130\}<310>_{\alpha''}$ twinning. A thin layer of ω phase is also observed at the β/α" inter-phase boundary. Occurrence of this unprecedented complex multi-step martensitic twinning process is rationalized by means of Schmid factor analysis and transformation strain calculations.

Keyword: superelastic titanium alloy, stress-induced martensitic transformation, twinning, plastic deformation.

* Corresponding author: philippe.castany@insa-rennes.fr

1. Introduction

Nowadays, metastable β titanium alloys are more and more used for biomedical applications owning to their numerous advantageous properties: low Young's modulus, high strength, good biocompatibility, attractive superelasticity and shape memory effect. The superelastic effect is activated through well-known reversible stress-induced martensitic (SIM) transformation between body-centered cubic (bcc) β phase and C-centered orthorhombic α″ martensitic phase [1-9]. With applied stress increasing, residual strain can be generated in the specimen due to plastic deformation.

Plastic deformation mechanisms are mainly dominated by dislocation glide [10-15] or deformation twinning [16-24] depending on parent β phase stability, while SIM transformation occurs as a first reversible deformation mechanism in superelastic alloys [1-9,13,19,22-23]. Dislocation glide was investigated through *in situ* straining TEM experiments in relatively more stable β titanium alloys [11-13]. With β phase stability decreasing, deformation twinning and stress-induced martensite are widely activated. In the case of superelastic alloys, extensive $\{332\}<113>_{\beta}$ twinning, and to a less extent $\{112\}<111>_{\beta}$ twinning, were frequently observed by EBSD and TEM in deformed specimens [9,22-27]. The reversible SIM α″ transformation was revealed with advanced *in situ* synchrotron X-ray diffraction technique during loading/unloading process and residual stress-induced martensite can finally be sometimes detected after unloading in the stage of plastic deformation [4-8,22-23,28-29].

Mechanisms of plastic deformation in SIM α″ phase are difficult to observe in superelastic β-Ti alloys due to the reversibility of SIM α″ phase transforming back to the parent β phase and to the spontaneous strain relaxation during the preparation of thin foils for TEM [7]. However, crystallographic reconstruction method, which is based on lattice correspondence between β and SIM α″ phases employed under the framework of the Phenomenological Theory of Martensite Crystallography (PTMC) [30-32] can be used to predict the actual martensitic twinning system operating on loading from the observed β phase [5,9,22-23]. According to the classical lattice correspondence from bcc β phase to orthorhombic α″ martensitic phase: $<100>_{\beta}$-$[100]_{\alpha''}$, $<011>_{\beta}$-$[010]_{\alpha''}$ and $<0\text{-}11>_{\beta}$-$[001]_{\alpha''}$, six equivalent corresponding variants (CV, designated as CV1 to CV6) can thus be formed from a single grain of β phase [24,33]. But when a tensile stress is applied, a variant selection occurs and only allows the nucleation and growth of CV which are preferentially orientated

regarding the applied stress direction. This method was successfully applied to explain the origin of {332}<113>$_\beta$ twinning [9,23], and {112}<111>$_\beta$ twinning [22,34] in superelastic Ti-based alloys from the reversion of {130}<310>$_{\alpha''}$ and {110}<110>$_{\alpha''}$ twins of SIM α″ phase, respectively. Deformation mechanisms of α″ phase can also be investigated in full α″ shape memory alloys, in which reverse SIM transformation does not occur after unloading. In such alloys, two types of twinning can be activated : (i) transformation or reorientation twinning, such as {111}$_{\alpha''}$ type I or <211>$_{\alpha''}$ type II twinning [24,31,33,35-36], occurring during the reorientation of self-accommodated α″ phase at the early stage of deformation and not related to plasticity as keeping the same β phase orientation after reverse transformation by heating, and (ii) deformation twinning occurring in the plastic deformation stage. For this later type, both predicted {130}<310>$_{\alpha''}$ and {110}<110>$_{\alpha''}$ twinning systems were respectively observed in bulk [24,37] and on the surface [38] of deformed shape memory full-α″ alloys. Two other deformation twinning systems were also observed: {103}<301>$_{\alpha''}$ compound twinning [37] and {315}'<121>'$_{\alpha''}$ type I twinning [35]. More recently, dislocations were also evidenced in α″ phase by TEM [39]. However, deformation mechanisms of α″ phase can slightly differ between superelastic alloys and full α″ shape memory alloys because of obviously different beta-stabilizing alloying element contents. Interactions between transformation twinning and deformation twinning in shape memory alloys could also modify the sequence of deformation.

The hexagonal ω phase was widely reported as one of the most significant non-equilibrium phases in metastable β titanium alloys. On one hand, thermal treatments can induce two types of ω phase formation: one is athermal ω_{ath} phase, which forms during rapid quenching from β phase domain [40-42]; the other one is isothermal ω_{iso} phase, which precipitates by low-temperature aging [43-46]. The formation of the forward mentioned thermal-assisted ω phases occurs by a displacive shuffle mechanism: two neighboring {111}$_\beta$ atoms layers of every three {111}$_\beta$ atoms layers collapse to each other into a middle plane position [40,47-48]. On the other hand, stress-induced ω phase is sometimes observed as a secondary deformation mechanism [49-50] or as interfacial ω phase lying on twin boundaries after stress releasing [51-53]. More recently, this stress-assisted ω phase along {332}<113>$_\beta$ or {112}<111>$_\beta$ twin boundaries was linked to reverse transformation from SIM α″ phase to β phase and the subsequent stress relaxation after unloading in Ti-Nb based superelastic alloys [9,22-23].

Literature widely reported plastic deformation mechanisms of β phase, specifically concerning $\{332\}<113>_{\beta}$ and $\{112\}<111>_{\beta}$ twinning systems, but investigations about deformation mechanisms in SIM α″ phase are still scarce for superelastic β titanium alloys due to the reverse martensitic transformation, while some mechanisms were evidenced in full α″ shape memory alloys. In this work, TEM observations are performed to reveal the plastic deformation microstructure of a Ti-20Zr-3Mo-3Sn alloy after tensile test. An abnormal orientation relationship between β phase and residual SIM α″ phase is observed, accompanied by interfacial ω phase along β/α″ phase boundaries. Based on crystallographic reconstruction and Schmid factor analysis, this observation is explained by a complex sequence composed of mechanical $\{130\}<310>_{\alpha''}$ twinning which is next reoriented by self-accommodation $\{111\}_{\alpha''}$ twinning, finally followed by a reverse α″ to β transformation of the matrix while α″ twins remain as residual α″ phase when the stress is removed.

2. Materials and methods

The Ti-20Zr-3Mo-3Sn alloy (at.%, Ti2033 for short) was synthesized by cold crucible levitation melting (CCLM) technique under argon atmosphere. For this synthesis, pure raw metals including 99.95% pure titanium, 99.078% pure zirconium, 99.9% pure molybdenum and 99.99% pure tin were used. After melting, ingot was homogenized at 950℃ for 1200 min under high vacuum (10^{-7} mbar), followed by water quenching. Then, the ingot was cold rolled until 95% reduction rate in thickness. Dog-bone tensile specimens were machined from the cold-rolled sheets with normalized shape: 3 mm width, 0.5 mm in thickness and a gage length of 15 mm. In order to restore a fully recrystallized microstructure from the cold-rolled state, the tensile specimens were finally short thermal treated at 700℃, which is above the β-transus temperature of 690℃ [4] for 2 min followed by water quenching. After that, all specimens were cleaned in an acid solution made of 50% HF and 50% HNO_3 (vol.%) to remove any oxidation layer.

Conventional and cyclic tensile tests with the strain rate of $10^{-4}s^{-1}$ were performed to evaluate mechanical properties. The tensile direction was chosen parallel to the cold rolling direction (RD), and an extensometer was used to measure the strain of the specimens accurately. For cyclic loading-unloading tensile tests, tensile stress was applied until the strain reached 0.5% for the first cycle, and then the load was removed. The measurement was then

repeated through increasing the strain by 0.5% steps upon loading until 5% of strain, and then followed by two steps until 6.0% and 8% of strain, each step being followed by unloading for the same specimen.

In order to characterize the microstructure after recrystallization at 700°C, electron back-scattered diffraction (EBSD) analysis was performed with a scanning electron microscope (Jeol JSM 7100F, SEM) equipped with an Oxford HKL EBSD system under the accelerating voltage of 20 kV and a step size of 0.1 μm. Prior to EBSD observations, the specimen was mechanically mirror-polished by using several SiC papers with decreasing grid size and followed by colloidal silica suspension (particles size: 0.05 μm). In this work, the colloidal silica suspension was mixed with H_2O_2 solution to release stress due to polishing and reveal the microstructure.

In situ synchrotron X-ray diffraction (SXRD) observation under cyclic tensile tests was carried out at the ID-22 high resolution powder diffraction beamline of the European Synchrotron Radiation Facility (ESRF, Grenoble, France) with a 1 mm^2 X-ray beam size and a 0.35453630 Å wavelength radiation. The *in situ* cyclic tensile tests were performed with increments of 0.5% until 5.0% of strain and then increased by 1.0% until 8.0% of strain during each loading and unloading condition at the strain rate of 10^{-4} s^{-1}. A nine-channel detector was used to collect transmitted diffracted beams for each cycle.

Transmission electron microscopy (TEM) observations were conducted using a JEOL 2100F microscope operating at 200 kV. Thin foils for TEM were firstly cut as 3 mm diameter disks and then mechanically polished to a thickness of 80 μm. Secondly, the polished samples were twin-jet electropolished with a solution of 6% perchloric acid and 94% methanol (vol.%) at -20°C and stopped before perforation. Finally, two-steps ion milling thinning was performed until perforation using successively 5 keV and 1 keV Ar ions with a Fischione 1010 Model.

3. Results

Fig.1a displays the initial SXRD profile of the investigated Ti2033 alloy after short solution treatment at 700°C for 2 min, and only typical β diffraction peaks are detected. The lattice parameter of β phase is measured as a_β=0.3333 nm. EBSD analyses are carried out to characterize the initial recrystallization texture induced by the heat treatment. Fig.1b is the EBSD inverse pole figure (IPF) map along the cold rolling direction. According to the color code, red, green and blue colors correspond respectively to $<001>_\beta$, $<101>_\beta$ and $<111>_\beta$ orientations paralleling to the cold-rolling direction. The sample has a full equiaxed β-grain microstructure with an average grain size of 1.5±1.1 μm and a large majority of grains are in green color indicating a strong $\{hkl\}<101>_\beta$ texture. In order to determine the recrystallized texture accurately, the orientation distribution function (ODF) is calculated for this sample, as shown in Fig.S1 in supplementary materials, and the corresponding IPFs are shown in Fig.1c. RD is the rolling direction (parallel to the tensile direction) and ND is the normal direction. The dominant $\{111\}<101>_\beta$ recrystallization texture is then confirmed from the IPF of Fig.1c.

Fig.2a shows the conventional and cyclic loading/unloading engineering tensile curves of the present Ti2033 alloy. From the conventional tensile curve, the mechanical characteristics of elongation at rupture, ultimate tensile strength and incipient Young's modulus can be measured as 8.5%, 945 MPa and 54 GPa, respectively. In the cyclic one, the presence of hysteresis between loading and unloading curves is attributed to the reversible SIM transformation between β and martensitic α" phases. The maximum superelastic recoverable strain is then measured to be 3.3%. One can also notice that in our previous work on the same alloy [4] a heat treatment was performed at the same temperature (700°C) but for 30 min instead of 2 min in the present study. This decrease of heat treatment time leads to a decrease of the average grain size and an increase of tensile strength, while keeping rather similar recoverable strain and texture, except for the ND direction which is more focused for a short heat treatment time. In order to highlight the SIM transformation during tensile tests, partial SXRD profiles near the most intense $(110)_\beta$ peak from 7.0° to 9.5°, including on loading and after unloading, at 5% and 8% of strains are illustrated in Fig.2b and 2c, respectively. On loading, the two samples only consist of SIM α" phase. After unlading, both residual SIM α" phase and reversed β phase are detected. The lattice parameters of SIM α" phase are measured as $a_{\alpha''}$=0.3124 nm, $b_{\alpha''}$=0.5050 nm, $c_{\alpha''}$=0.4738 nm. Besides, the entire

SXRD profiles (2θ range of 5-18°) at 5% and 8% of strains are also provided in Fig.S2 in supplementary materials.

For the plastic deformation microstructure observation, two samples were taken from interrupted tensile tests: one at 5% of strain and the other one at 8% nearly rupture, as shown in Fig.2a. Fig.3a presents a TEM bright-field image obtained from the sample at 5% of strain. A nano-sized deformation band with width of about 50 nm is observed nearly edge-on. Fig.3b shows the corresponding selected area electron diffraction (SAED) pattern captured on the boundary of the band and the matrix (white circle in Fig.3a). After indexation (Fig.3c), the stress-induced deformation band is identified as martensitic α" phase with orthorhombic structure (space group N°63, Cmcm), with the $[-12-1]_{\alpha"}$ zone axis nearly parallel to $[1-1-1]_{\beta}$ zone axis, which is consistent with SXRD result of Fig.2b. Fig.3d and 3e show dark-field images for parent β phase and SIM α" phase taken with the spot marked with a red circle and the spot marked with a green circle on SAED pattern of Fig.3b, respectively. Surprisingly, the observed orientation relationship (OR) between β matrix and SIM α" phase is not the usual one, for which a $<111>_{\beta}$ zone axis should be parallel to a $<110>_{\alpha"}$ or a $<101>_{\alpha"}$ direction of α" martensite [4,24,33]. For more details, the conventional OR is shown in Fig.S3 and compared to the observed orientation in supplementary materials. Another diffracting condition with $[100]_{\beta}$ nearly parallel to $[110]_{\alpha"}$ zone axis is also provided in supplementary materials (Fig.S4) to support the new observed OR. This unusual OR will be discussed in more details by the examination of stereographic projections in the section 4.1.

When the Ti2033 alloy is deformed to 8% of strain, a much more complex deformation microstructure is obtained, as shown in the TEM bright-field image of Fig.4a. A large deformation band is observed with some parallel nano-sized bands inside. In order to firstly identify the components of this hierarchical microstructure, a SAED pattern focusing inside the large deformation band (yellow circle in Fig.4a) is obtained in Fig.4b. It reveals two crystallographic orientations of SIM α" phase sharing a common $<110>_{\alpha"}$ zone axis: $[1-10]_{\alpha"\text{-prim}} \| [-110]_{\alpha"\text{-sec}}$, in which α"-prim and α"-sec refer to primary α" band and secondary α" band, respectively. Fig.4c-f show the key diagram of SAED pattern and several dark-field images. The dark-field images in Fig.4d, Fig.4e and Fig.4f are imaged from the diffraction spots marked by green, purple and yellow circles in Fig.4b, respectively. As it will be justified from the detailed analysis in the next section, the small bands with width of 20-30 nm highlighted in Fig.4d are designated as primary α" bands and the largest band with width of ~300nm

highlighted in Fig.4e is labeled as secondary α" band. The Fig.4f shows the dark field image taken with the common $(11\text{-}1)_{\alpha''}$ spot of both primary and secondary bands. Both β and SIM α" phases are simultaneously detected by TEM and SXRD (Fig.2c) techniques, showing a good agreement in our observations.

In addition, Fig.5 displays another diffracting condition of the same deformation band than in Fig.4. The SAED pattern of Fig.5a is obtained from the area circled in green in Fig.4a. It reveals the presence of parent β phase, both primary and secondary SIM α" phase and ω phase with the following zone axis nearly parallel: $[113]_{\beta}\|[7\text{-}5\text{-}2]_{\alpha''\text{-prim}}\|[\text{-}210]_{\alpha''\text{-sec}}\|[1\text{-}213]_{\omega}$. A SAED pattern taken from the β matrix only is also provided for a better readability in Fig.5b for the same orientation. Fig.5c is a key diagram of the SAED patterns of Fig.5a-b. Moreover, the presence of ω phase can be unambiguously established due to the presence of the $(\text{-}1010)_{\omega}$ spot that cannot be attributed to any other phase of titanium alloys. Fig.5d-f present dark-field images, which are imaged from the diffraction spots marked by red, green and yellow circles in Fig.5a, respectively. Fig.5d shows then β matrix and ω phase, and Fig.5e highlights both primary and secondary martensitic α" phase with also ω phase. Finally, Fig.5f only shows ω phase and allows to observe its localization at the phase boundary between β phase and α" martensitic phase, as the highlighted parts in Fig.5f correspond to common parts of matrix (Fig.5d) and twin (Fig.5e). Then, only an interfacial phase can explain this observation. It can be noticed that this interfacial layer of ω phase appears here rather thick (Fig.5f) because the interface is far from an edge-on condition, but it was not possible to bring this interface edge-on due to the orientation of the present twin. Such interfacial ω phase was already reported in literature along twin boundaries separating two crystals of β phase [9,22-23,52-53] but never observed between β and α" phases. Meanwhile, the OR between β and ω phases is found from Fig.5a to be the classical OR [41] as:

$$\{1101\}_{\omega}\|\{110\}_{\beta},\ \{0001\}_{\omega}\|\{111\}_{\beta},\ \langle 11\text{-}20\rangle_{\omega}\|\langle 110\rangle_{\beta}$$

And the OR between α" and ω phases is found as:

$$\{1101\}_{\omega}\|\{002\}_{\alpha''},\ \{0001\}_{\omega}\|\{205\}_{\alpha''},\ \langle 11\text{-}20\rangle_{\omega}\|\langle 512\rangle_{\alpha''}$$

The observed OR between β matrix and SIM α" phase is still abnormal and will be discussed in details from stereographic projections in section 4.1.

4. Analysis and Discussion

4.1. Identification of orientation relationships

The superelastic effect is due to the reversible transformation between initial bcc β phase and orthorhombic SIM α" phase in metastable β Ti-based alloys. With the strain increasing, some irreversible α" phase can be detected due to the onset of plastic deformation. As shown in the previous section, unprecedented OR between β and α" phases is found in deformed specimens. In order to elucidate the origin of such OR between observed β phase and SIM α" phase, the crystallographic reconstruction method, which is based on the lattice correspondence between β phase and SIM α" phase, is used to (i) predict the crystallographic orientation of SIM α" phase actually formed under stress and (ii) determine the potential martensitic twinning systems really activated on loading in SIM α" phase. From a known crystallographic orientation of β matrix, the six possible corresponding variants (CV) of α" phase can be reconstructed [4,22-24,31,33]. Among these six CV, the variant with the maximum calculated transformation strain is assumed to be the real activated one during loading. Then, twinning in this CV can be analyzed. This method will be used to explain the observed OR in both specimens deformed at 5% and 8% of strains.

The crystallographic orientations of β matrix and deformation band observed in Fig.3 in the specimen strained to 5% are shown on stereographic projections in Fig.6a and Fig.6e, in which solid circles represent poles of crystallographic planes and open circles represent crystallographic directions. For a better readability, only the three $\{100\}_{\beta/\alpha''}$ poles and some other related poles and traces of interest are presented. It is worth noting that the OR between β and α" phases (Fig.6a and Fig.6e) is not the conventional one with $(100)_{\alpha''} \| \{100\}_{\beta}$ and $[101]_{\alpha''} \| <111>_{\beta}$ [4,24,33], as shown in Fig.S3a-b in supplementary materials. This means that the plate of α" martensite was not formed directly from parent β phase under loading because it does not correspond to one of the six possible CV related to this β phase orientation. Another mechanism leading to the loss of the initial OR has then occurred. This unexpected feature is explained hereafter.

In order to determine the real activated martensite variant, values of transformation strain are calculated according to the orientation of the β matrix with the tensile direction $[3,23,-24]_{\beta}$ (Fig.6a) for each CV of α" martensite, as shown in Table 1. From this result, one can notice that CV2 offers obviously the maximum of transformation strain of 7.03% and has to be

formed during deformation for the specimen strained to 5%. Let's then assume that this CV2 is initially formed during tensile test and is not observed due to the reversibility of the SIM transformation. Its crystallographic orientation is reported in Fig.6c. To find the observed crystallographic orientation of α" martensite, this CV2 has to be transformed by deformation twinning. As the trace of the $(1\text{-}30)_{\alpha''}$ plane is parallel to the interface of the α" plate on the Fig.3a, this plane can be the twinning plane of the well-known $\{130\}\langle 310\rangle_{\alpha''}$ twinning system [9,23,24,37]. This potential twinning system, which is able to produce the actual orientation of α" phase, is then searched by applying a rotation of 180° around either potential twinning plane $(1\text{-}30)_{\alpha''}$ or twinning direction $[310]_{\alpha''}$. The result of this operation is shown on Fig.6d, but it does not correspond to the observed crystallographic orientation of the α" plate (Fig.5e). Other known twinning systems are also unsuccessfully tested. But as the $(1\text{-}30)[310]_{\alpha''}$ twin has a great correspondence with the observed interface orientation, one can then assume that this twin could be twinned again. To check this hypothesis, common poles are searched between the $(1\text{-}30)[310]_{\alpha''}$ twin (Fig.6d) and the observed α" plate (Fig.6e). A common $\{111\}_{\alpha''}$ pole is then found and a rotation of 180° around this $(\text{-}111)_{\alpha''}$ pole in Fig.6d turns out to be the Fig.6e. In other words, the OR between Fig.6d and Fig.6e is proved to be the well-known self-accommodation $\{111\}_{\alpha''}$ type I twinning system [24,31,33]. It will be labeled as reorientation twinning in the following because the corresponding orientation of β phase is unchanged after applying such a $\{111\}_{\alpha''}$ twinning system. Finally, the unusual OR between the observed α" plate and the β matrix in the specimen strained to 5% is due to occurrence of a two-step twinning of the SIM α" phase: After SIM transformation of the β matrix into the CV2 of α" martensite, a first mechanical $\{130\}\langle 310\rangle_{\alpha''}$ twinning occurs; Then, this mechanical twin undergoes another twinning process through reorientation $\{111\}_{\alpha''}$ twinning. This two-stage plastic deformation phenomenon was never reported in superelastic titanium alloys and will be supported in the next section from Schmid factor analysis. Moreover, the $\{130\}\langle 310\rangle_{\alpha''}$ twin corresponds to a $\{332\}\langle 113\rangle_{\beta}$ twin by applying the OR between β and α" phases as previously reported [9,19,23,24,37] with the $(2\text{-}33)_{\beta}$ twinning plane and the $[31\text{-}1]_{\beta}$ twinning direction (Fig.6a-b). But due to the occurrence of complete $\{111\}_{\alpha''}$ reorientation twinning of the initial $\{130\}\langle 310\rangle_{\alpha''}$ twin, this correspondence is lost, even if the crystallographic orientation of β phase is unchanged. Indeed, if the observed α" plate was reversed back to β phase, it would also correspond to a $\{332\}\langle 113\rangle_{\beta}$ twin, but without the correspondence with $\{130\}\langle 310\rangle_{\alpha''}$ twinning. This would then correspond to another correspondence with a $\{315\}\langle 121\rangle_{\alpha''}$ twinning system, which was very recently observed in a full α" shape memory alloy [35]. Another route to explain the observed OR

could then be the direct activation of such $\{315\}\langle 121\rangle_{\alpha''}$ twinning system, but it would mean that the CV4 would be formed as a first step of deformation instead of CV2. As CV4 would lead to a compression of the crystal (negative transformation strain value in Table 1), this scenario is unlikely to occur. The two-step process composed of $\{130\}\langle 310\rangle_{\alpha''}$ twinning followed by $\{111\}_{\alpha''}$ reorientation twinning is then the sole possibility to explain the observed OR and can also be an alternative route to explain the observation of $\{315\}\langle 121\rangle_{\alpha''}$ twins. Contrarily to what is commonly observed in superelastic Ti-based alloys in which $\{332\}\langle 113\rangle_{\beta}$ twins are observed after reverse SIM transformation [9,17,18,20,23,24,27] occurrence of additional $\{111\}_{\alpha''}$ reorientation twinning seems then to impede the reversion of martensitic twins into β phase in the present Ti2033 alloy.

In order to clarify the OR of the complex hierarchically twinned microstructure in Fig.4 and Fig.5, the same method is applied on the 8% deformation sample. The crystallographic orientations of the observed β-matrix, α"-primary band and α"-secondary band obtained from SAED patterns are represented by stereographic projections in Fig.7a, Fig.7d and Fig.7f, respectively. The six possible α" CV are deduced from parent β matrix and transformation lattice strains are calculated for each CV (Table 1). Then, CV6 offers the highest transformation strain of 5.86% and is the one assumed to be really formed under loading. Its stereographic projection, corresponding then to α" matrix, is shown in Fig.7c. This α"-matrix in Fig.7c clearly shares a common $\{130\}_{\alpha''}$ pole and a common $\langle 310\rangle_{\alpha''}$ direction with the observed α"-primary band in Fig.7d, which highlights the occurrence of $\{130\}\langle 310\rangle_{\alpha''}$ twinning as reported for the specimen strained to 5%. The operation of a reflection on the $(130)_{\alpha''}$ plane or a rotation of 180° around the $[3\text{-}10]_{\alpha''}$ direction of the α"-primary crystal leads to the orientation of the observed α"-primary band, confirming the twinning relationship. The $(130)_{\alpha''}$ twinning plane and $[3\text{-}10]_{\alpha''}$ twinning direction in martensitic α" phase also coincide with $(3\text{-}32)_{\beta}$ plane and $[\text{-}113]_{\beta}$ direction in Fig.7a, respectively. The corresponding β-twin is then constructed in Fig.7b. This first step is in agreement with the specimen deformed at 5% and confirms that the small bands observed in Fig.4 are actually the primary plastic deformation product during straining.

In terms of the OR between the primary and secondary bands for the 8% deformation sample, no direct twinning OR between Fig.7d and Fig.7f can be observed even if the $(11\text{-}1)_{\alpha''}$ pole is nearly common and leads to an apparent twinning relationship in the SAED pattern of Fig.4b. Indeed, a rotation of 180° around this pole $(11\text{-}1)_{\alpha''}$ in Fig.7d does not conduct to the

crystallographic orientation of Fig.7f. However, as observed in the 5% deformed specimen, one can assume that the primary $\{130\}<310>_{\alpha''}$ twin is totally reorientated by $\{111\}_{\alpha''}$ twinning. By testing the four possible $\{111\}_{\alpha''}$ twinning systems, i.e. constructing the four stereographic projections after the rotation of 180° around each $\{111\}_{\alpha''}$ pole of Fig.7d, only one possibility gives a crystallographic orientation with a twinning OR with the observed α"-secondary band in Fig.7f. This result is shown in Fig.7e in which the $(11\text{-}1)_{\alpha''}$ pole is common with the observed α"-primary band in Fig.7d. Then, common $\{130\}_{\alpha''}$ plane and $<310>_{\alpha''}$ direction are detected between Fig.7e and Fig.7f. In the same way, an operation of 180° rotation around $(-130)_{\alpha''}$ pole or $[310]_{\alpha''}$ direction of Fig.7e leads to the crystallographic orientation of the observed α"-secondary band of Fig.7f. And this twinning operation keeps the common $(11\text{-}1)_{\alpha''}$ pole almost at the same position in Fig.7f, explaining the apparent twinning relationship observed in the SAED pattern of Fig.4b. Therefore, the hierarchical microstructure observed in the specimen strained to 8% is due to a three-step twinning process composed of a primary $\{130\}<310>_{\alpha''}$ twinning of α" matrix, followed by a full reorientation by $\{111\}_{\alpha''}$ twinning, which is finally totally twinned again by a secondary $\{130\}<310>_{\alpha''}$ twinning. This complex twinning process was never observed in superelastic Ti-based alloys and will be rationalized in the next section.

4.2. Schmid factor analysis

The Schmid Factor (SF) is defined as $SF=\cos\lambda\cdot\cos\varphi$, where λ is the angle between the tensile direction and the normal direction of the twinning plane K_1, and φ is the angle between the tensile direction and the twinning direction η_1. The values of λ and φ angles are both between 0^o and 180^o and the calculated SF values thus lie between -0.5 and 0.5, in which negative values would result in a contraction of the crystal and positive values result in an elongation of the crystal accommodating then a tensile stress along the tensile direction [17,23-24,54].

The activation of $\{130\}<310>_{\alpha''}$ twinning system in α" phase is firstly investigated by this SF analysis method for the 5% deformation specimen. The tensile direction is $[2,25,-1]_{\alpha''}$ in the α" matrix (after full β to α" SIM transformation) and then SF values are listed for the two variants in Table 2 (column SF(1)). Both variants have a high SF value and the one with the highest SF value (0.44, which is highlighted in red in Table 2) is the one expected to be

activated in the previous section. Let's now explain why this (1-30)[-3-10]$_{\alpha''}$ twin is further reorientated by a {111}$_{\alpha''}$ twinning system. The parent β phase deduces from this (1-30)[-3-10]$_{\alpha''}$ twin is shown in Fig.6b and corresponds to a {332}<113>$_{\beta}$ twin regarding the β matrix according the relationship between these twinning systems in both β and SIM α" phases [9,23,24,37]. The orientation of the (1-30)[-3-10]$_{\alpha''}$ twin corresponds then to the CV2 (Fig.6d) regarding the β-twin (Fig.6b). If transformation strains are calculated along [-15,6,-5]$_{\beta}$ for each CV regarding this β phase orientation (second column in Table 1), the CV2 can obviously not optimally accommodate the applied strain as its negative value means a compression of the crystal along the tensile direction. That is why this twin undergoes a {111}$_{\alpha''}$ reorientation twinning process to be transformed into the observed orientation of α" phase (Fig.6e) that is the CV4. This additional step allows accommodation of a larger strain than simple {130}<310>$_{\alpha''}$ twinning. Even if CV4 indeed allows an elongation of the crystal (positive value in Table 1), it is quite surprising to not rather observed a reorientation into CV3 or CV6 which are more favorable and could be formed by other variants of the {111}$_{\alpha''}$ twinning system. An explanation could be internal local stresses promoting twin variants which are not the most favorable relative to the macroscopic tensile stress. Compatibility stresses between neighboring grains can also explain this feature, especially in the present alloy with very small grain size. Further investigations are needed to completely rationalize the activation of reorientation twinning observed after primary {130}<310>$_{\alpha''}$ twinning.

At 8% deformation, the same method is conducted and the result is shown in Table 2: The column SF(2) corresponds to SF values of the primary {130}<310>$_{\alpha''}$ twinning in the α" matrix of Fig.7c with the [3,-23,12]$_{\alpha''}$ tensile direction and the column SF(3) corresponds to SF values of the secondary {130}<310>$_{\alpha''}$ twinning in the α" reorientated twin of Fig.7e with the [8,4,-5]$_{\alpha''}$ tensile direction. The first steps of deformation are similar to the 5% strained specimen with activation of the {130}<310>$_{\alpha''}$ twin variant of highest SF value in the α" matrix (0.37 in red in Table 2) followed by a reorientation via {111}$_{\alpha''}$ twinning. Similarly, the primary {130}<310>$_{\alpha''}$ twin corresponds to a compression variant (CV6 in the fourth column of Table 1) and is reorientated to a variant in tension (CV1) which is not the one with the highest transformation strain. Until this step, the sequence follows exactly the same steps than in the specimen strained to 5%, except that some residual parts of the primary {130}<310>$_{\alpha''}$ twin are still present in the microstructure (small bands highlighted in Fig.4d). However, another step is activated in the 8% strained specimen that leads to the main observed orientation (Fig.4e and Fig.7f). This crystallographic orientation is then obtained

after a secondary {130}<310>$_{\alpha''}$ twinning of the primary reorientated twin. According to SF analysis (column SF(3) in Table 2), the activated {130}<310>$_{\alpha''}$ twin variant is the one with the highest positive SF value, even if this value is very low (0.10). This last twinning process extensively occurs to almost totally twin the primary reoriented twin.

4.3. Sequence of plastic deformation

The full β microstructure with <101>$_{\beta}$ type texture is formed in the Ti2033 alloy after recrystallization treatment. When the tensile stress is applied, a complex sequence of plastic deformation mechanisms is progressively activated. This sequence is summarized in Fig.8 and discussed hereafter.

As evidenced from SXRD experiments (Fig.2), all the β phase is first totally transformed into SIM α" phase on loading. The CV of α" martensite leading to the highest transformation strain is the one activated until all the initial β grains transform into a single martensitic variant. Once the load is removed, this SIM α" phase transforms back to β phase leading to the total recovery of applied strain during the tensile test.

When the stress increases, {130}<310>$_{\alpha''}$ twins are first activated leading to unrecoverable plastic deformation. Such twins are commonly thought to occur in superelastic Ti-based alloys as precursors to {332}<113>$_{\beta}$ twins observed after deformation [9,19,23,24,27,37] and were recently directly observed in Transformation Induced Plasticity (TRIP) alloys [55-58]. The variant selection of the observed {130}<310>$_{\alpha''}$ twins obeys the Schmid law. Once nucleated and grown, these primary {130}<310>$_{\alpha''}$ twins are reorientated via {111}$_{\alpha''}$ twinning (Fig.8a). After unloading, the α" matrix transforms back to β phase while the reorientated primary twins remain (Fig.8b). This step corresponds to the specimen deformed at 5% (Fig.3) and leads to an abnormal OR between β and SIM α" phases. This sequence is quite different to what is commonly observed in Ti-based superelastic alloys in which such {130}<310>$_{\alpha''}$ twins are not subject to {111}$_{\alpha''}$ reorientation twinning and transform back to {332}<113>$_{\beta}$ twins after unloading [9,19,23,24,27,37]. One can also notice that similar reorientation of {130}<310>$_{\alpha''}$ twins was observed in a full-α" shape memory alloy [24], but via the <211>$_{\alpha''}$ type II reorientation twinning instead of the present {111}$_{\alpha''}$ type I. Nevertheless, such reorientation process was never observed in superelastic alloys.

Regarding the tensile curve (Fig.2a), about 2% of residual strain remain after unloading and the presence of such twins participate to this unrecoverable strain. Residual strain is also due to the presence of dislocations that are visible in the matrix of Fig.3a and Fig.3d. However, superelasticity (3.2%) is still high at this stage of deformation as shown by the presence of β phase as the main phase in TEM observations (Fig.3) and SXRD results (Fig.2b and Fig.S2a), showing the reversibility of SIM transformation.

If the applied stress further increases, the reorientated primary $\{130\}\langle 310\rangle_{\alpha''}$ twins undergo a secondary $\{130\}\langle 310\rangle_{\alpha''}$ twinning (Fig.8c), which also obeys the Schmid law. This step corresponds to the specimen observed after 8% of strain (Fig.4 and Fig.5). After unloading, the α" matrix still transforms back to β phase and the twinned α" bands remain (Fig.8d). This step also leads to an abnormal OR between β and α" phases. However, contrarily to 5% specimen, an interfacial thin layer of ω phase lies along the phase boundary (Fig.5f). This interfacial ω phase layer is thought to be formed to accommodate internal stresses due to abnormal β/α" OR during unloading. Such interfacial ω phase layer was previously reported along twin boundaries [9,23] and its formation during unloading was evidenced from SXRD experiments [22]. This ω phase layer is not observed in the specimen strained to 5%, most probably because the β/α" OR does not lead to strong internal stresses when secondary $\{130\}\langle 310\rangle_{\alpha''}$ twinning does not occur. Such secondary $\{130\}\langle 310\rangle_{\alpha''}$ twinning inside primary reorientated twins was never observed before. At this stage of deformation, superelasticity is strongly reduced to only 1.8% (Fig.2a) due to the increase of plastic deformation, highlighted here by the growth of primary twins and nucleation of secondary twins, which decreases the reversibility of SIM transformation.

This complex twinning process was never reported before in superelastic Ti-based alloys and presents several differences with previous studies. First of all, twins are generally wider (up to several microns) without internal secondary twinning [9,13,17,20-27], while their size does not exceed 200 nm in the present alloy and undergoing several steps of twinning. This feature highlights a higher critical stress to grow the twins instead of other Ti-Nb based alloys in which the growth of twins is easier. And even if massive secondary twinning is sometimes observed in some Ti-Nb alloys [23] only secondary $\{130\}\langle 310\rangle_{\alpha''}$ twinning was evidenced and full reorientation of primary twins via $\{111\}_{\alpha''}$ twinning was never reported. Thus, it seems energetically more favorable in the present Ti2033 alloy to twin again primary twins via $\{111\}_{\alpha''}$ reorientation twinning instead of their growth. In other words, it is easier to

reorientate than to grow primary $\{130\}<310>_{\alpha''}$ twins in the present Ti-Zr based alloy, while the contrary occurs in Ti-Nb based alloys, allowing then the observation of micron-scale twins instead of nano-scale twins. It can also be noticed that such $\{111\}_{\alpha''}$ reorientation process seems to impede the reversion of the twin into β phase, and, in turn, the observation of $\{332\}<113>_{\beta}$ twins after unloading. Such reorientation twinning process has then an important effect on the observed deformation microstructures that are definitively different to what is commonly observed in Ti-Nb based superelastic alloys: α″ plates with unconventional OR are observed instead of $\{332\}<113>_{\beta}$ twins. This change in the sequence of deformation is then most probably due to the replacement of Nb by Zr as the main alloying element and could occur in all newly-developed Ti-Zr based superelastic or TRIP alloys [4,8,29,59-61] as well as in Ti-Hf alloys [28,62] or Ti-based high entropy alloys (HEA) [63-64]. Evidence of this complex sequence of plastic deformation would allow a better understanding of deformation microstructures in Ti-Zr based alloys and unravel observations of abnormal β/α" OR.

Finally, it also can be noticed that the ductility of the present alloy (8.5%) is slightly lower than that of classical Ti-Nb superelastic alloys, whose ductility reaches about 10-15% [1,7,65]. This feature can be explained again by the low twin growth, due to the replacement of Nb by Zr as main alloying element, that decreases the capability of deformation and then the ductility of the present alloy. Indeed, twins are usually very large in Ti-Nb alloys [9,13,17,20-27] reaching several tens of micrometers of width, while twin width does not exceed few hundreds of nanometers in the present study (Fig.4) for an applied strain near the rupture of the specimen.

5. Conclusion

In the present investigation, the Ti2033 alloy is studied after short solution treatment by means of conventional and cyclic tensile tests, EBSD, SXRD and TEM before and after deformation. A complex multi-step sequence of plastic deformation is evidenced from TEM observations of specimens strained to 5% and 8%. The main conclusions can be summarized as followings:

(1) SIM transformation first occurs. Each β grain is transformed into the α" CV with the highest transformation strain. The full reversion of SIM transformation leads to superelasticity, as observed by SXRD experiments.

(2) Once plastic deformation starts, $\{130\}\langle 310\rangle_{\alpha''}$ twins are nucleated in α" matrix. The activated variant is the one with the highest SF value. Then, such primary $\{130\}\langle 310\rangle_{\alpha''}$ twins are subject to a reorientation process, which was never reported before, via $\{111\}_{\alpha''}$ reorientation twinning until their complete reorientation. After unloading, these reorientated α" twins remain while the α" matrix transforms back to β phase. This step leads to an abnormal OR between β and α" phases and corresponds to the specimen observed after 5% of strain.

(3) When the applied strain increases further, secondary $\{130\}\langle 310\rangle_{\alpha''}$ twinning occurs inside the former primary reorientated $\{130\}\langle 310\rangle_{\alpha''}$ twins. This complex multi-step deformation sequence is evidenced for the first time in a Ti-based superelastic alloy. Secondary twinning also obeys the Schmid law. After unloading such complex twinned bands remain in the β matrix with an abnormal β/α" OR. An interfacial layer of ω phase also appears at the interphase boundary to accommodate internal stresses during unloading.

(4) $\{111\}_{\alpha''}$ reorientation twinning occurs because: (i) primary $\{130\}\langle 310\rangle_{\alpha''}$ twins does not correspond to the CV with the highest transformation strain but to compression CV and (ii) the growth of these twins is energetically more difficult than in Ti-Nb based alloys reported in literature. However, the reorientated variant formed via $\{111\}_{\alpha''}$ twinning is never the one leading to the highest transformation strain. Internal local stresses are most probably the reason of this deviation from theoretical assumption.

(5) The $\{111\}_{\alpha''}$ reorientation twinning of primary $\{130\}\langle 310\rangle_{\alpha''}$ twins also impedes the reversion of twins into β phase after unloading as commonly observed in Ti-Nb based superelastic alloys. As a consequence, the superelasticity is slightly reduced from this phenomenon and it could then further be increased by a better understanding of such mechanism.

Acknowledgement

J. J. Gao acknowledges the China Scholarship Council (CSC) for his Ph.D financial support (No.2016-6329). The authors also acknowledge respectively the THEMIS and CMEBA platforms of the University of Rennes, as well as ESRF (Grenoble, France) for providing access to the TEM, SEM-EBSD and SXRD facilities.

References

[1] H.Y. Kim, Y. Ikehara, J.I. Kim, H. Hosoda, S. Miyazaki, Martensitic transformation, shape memory effect and superelasticity of Ti–Nb binary alloys, Acta Materialia. 54 (2006) 2419–2429. https://doi.org/10.1016/j.actamat.2006.01.019.

[2] M. Tahara, H.Y. Kim, H. Hosoda, S. Miyazaki, Cyclic deformation behavior of a Ti–26 at.% Nb alloy, Acta Materialia. 57 (2009) 2461–2469. https://doi.org/10.1016/j.actamat.2009.01.037.

[3] Y. Al-Zain, H.Y. Kim, T. Koyano, H. Hosoda, T.H. Nam, S. Miyazaki, Anomalous temperature dependence of the superelastic behavior of Ti–Nb–Mo alloys, Acta Materialia. 59 (2011) 1464–1473. https://doi.org/10.1016/j.actamat.2010.11.008.

[4] J.J. Gao, I. Thibon, D. Laillé, P. Castany, T. Gloriant, Influence of texture and transformation strain on the superelastic performance of a new Ti–20Zr–3Mo–3Sn alloy, Materials Science and Engineering: A. 762 (2019) 138075. https://doi.org/10.1016/j.msea.2019.138075.

[5] E.G. Obbard, Y.L. Hao, T. Akahori, R.J. Talling, M. Niinomi, D. Dye, R. Yang, Mechanics of superelasticity in Ti–30Nb–(8–10)Ta–5Zr alloy, Acta Materialia. 58 (2010) 3557–3567. https://doi.org/10.1016/j.actamat.2010.02.010.

[6] P. Castany, A. Ramarolahy, F. Prima, P. Laheurte, C. Curfs, T. Gloriant, In situ synchrotron X-ray diffraction study of the martensitic transformation in superelastic Ti–24Nb–0.5N and Ti–24Nb–0.5O alloys, Acta Materialia. 88 (2015) 102–111. https://doi.org/10.1016/j.actamat.2015.01.014.

[7] Y. Yang, P. Castany, M. Cornen, F. Prima, S.J. Li, Y.L. Hao, T. Gloriant, Characterization of the martensitic transformation in the superelastic Ti–24Nb–4Zr–8Sn alloy by in situ synchrotron X-ray diffraction and dynamic mechanical analysis, Acta Materialia. 88 (2015) 25–33. https://doi.org/10.1016/j.actamat.2015.01.039.

[8] J.J. Gao, I. Thibon, P. Castany, T. Gloriant, Effect of grain size on the recovery strain in a new Ti–20Zr–12Nb–2Sn superelastic alloy, Materials Science and Engineering: A. 793 (2020) 139878. https://doi.org/10.1016/j.msea.2020.139878.

[9] P. Castany, Y. Yang, E. Bertrand, T. Gloriant, Reversion of a parent {130}⟨310⟩α″ martensitic twinning system at the origin of {332}⟨113⟩β twins observed in metastable β titanium alloys, Physical Review Letters 117 (2016) 245501. https://doi.org/10.1103/PhysRevLett.117.245501.

[10] Y. Kamimura, S. Katakura, K. Edagawa, S. Takeuchi, S. Kuramoto, T. Furuta, Thermally activated deformation of gum metal: A strong evidence for the Peierls mechanism of deformation, Materials Transactions. 56 (2015) 2084–2087. https://doi.org/10.2320/matertrans.M2015271.

[11] P. Castany, M. Besse, T. Gloriant, Dislocation mobility in gum metal β-titanium alloy studied via in situ transmission electron microscopy, Physical Review B 84 (2011) 020201. https://doi.org/10.1103/PhysRevB.84.020201.

[12] P. Castany, M. Besse, T. Gloriant, In situ TEM study of dislocation slip in a metastable β titanium alloy, Scripta Materialia. 66 (2012) 371–373. https://doi.org/10.1016/j.scriptamat.2011.11.036.

[13] P. Castany, D.M. Gordin, S.I. Drob, C. Vasilescu, V. Mitran, A. Cimpean, T. Gloriant, Deformation mechanisms and biocompatibility of the superelastic Ti–23Nb–0.7Ta–2Zr–0.5N alloy, Shap. Mem. Superelasticity. 2 (2016) 18–28. https://doi.org/10.1007/s40830-016-0057-0.

[14] M.J. Lai, C.C. Tasan, D. Raabe, Deformation mechanism of ω-enriched Ti–Nb-based gum metal: Dislocation channeling and deformation induced ω–β transformation, Acta Materialia. 100 (2015) 290–300. https://doi.org/10.1016/j.actamat.2015.08.047.

[15] E. Farghadany, A. Zarei-Hanzaki, H.R. Abedi, D. Dietrich, M.R. Yadegari, T. Lampke, The coupled temperature–strain rate sensitivity of Ti–29Nb–13Ta–4.6Zr alloy, Materials Science and Engineering: A. 610 (2014) 258–262. https://doi.org/10.1016/j.msea.2014.04.052.

[16] H. Zhan, W. Zeng, G. Wang, D. Kent, M. Dargusch, On the deformation mechanisms and strain rate sensitivity of a metastable β Ti–Nb alloy, Scripta Materialia. 107 (2015) 34–37. https://doi.org/10.1016/j.scriptamat.2015.05.014.

[17] E. Bertrand, P. Castany, I. Péron, T. Gloriant, Twinning system selection in a metastable β-titanium alloy by Schmid factor analysis, Scripta Materialia. 64 (2011) 1110–1113. https://doi.org/10.1016/j.scriptamat.2011.02.033.

[18] M. Ahmed, D. Wexler, G. Casillas, O.M. Ivasishin, E.V. Pereloma, The influence of β phase stability on deformation mode and compressive mechanical properties of Ti–10V–3Fe–3Al alloy, Acta Materialia. 84 (2015) 124–135. https://doi.org/10.1016/j.actamat.2014.10.043.

[19] H. Tobe, H.Y. Kim, T. Inamura, H. Hosoda, S. Miyazaki, Origin of {332} twinning in metastable β–Ti alloys, Acta Materialia. 64 (2014) 345–355. https://doi.org/10.1016/j.actamat.2013.10.048.

[20] S. Hanada, O. Izumi, Transmission electron microscopic observations of mechanical twinning in metastable beta titanium alloys, Metallurgical Transactions A. 17 (1986) 1409–1420. https://doi.org/10.1007/BF02650122.

[21] T. Kawabata, S. Kawasaki, O. Izumi, Mechanical properties of TiNbTa single crystals at cryogenic temperatures, Acta Materialia. 46 (1998) 2705–2715. https://doi.org/10.1016/S1359-6454(97)00475-8.

[22] Y. Yang, P. Castany, E. Bertrand, M. Cornen, J.X. Lin, T. Gloriant, Stress release-induced interfacial twin boundary ω phase formation in a β type Ti–based single crystal displaying stress-induced α″ martensitic transformation, Acta Materialia. 149 (2018) 97–107. https://doi.org/10.1016/j.actamat.2018.02.036.

[23] Y. Yang, P. Castany, Y.L. Hao, T. Gloriant, Plastic deformation via hierarchical nano-sized martensitic twinning in the metastable β Ti–24Nb–4Zr–8Sn alloy, Acta Materialia. 194 (2020) 27–39. https://doi.org/10.1016/j.actamat.2020.04.021.

[24] E. Bertrand, P. Castany, Y. Yang, E. Menou, T. Gloriant, Deformation twinning in the full-α″ martensitic Ti–25Ta–20Nb shape memory alloy, Acta Materialia. 105 (2016) 94–103. https://doi.org/10.1016/j.actamat.2015.12.001.

[25] R.J. Talling, R.J. Dashwood, M. Jackson, D. Dye, On the mechanism of superelasticity in Gum metal, Acta Materialia. 57 (2009) 1188–1198. https://doi.org/10.1016/j.actamat.2008.11.013.

[26] M. Besse, P. Castany, T. Gloriant, Mechanisms of deformation in gum metal TNTZ–O and TNTZ titanium alloys: A comparative study on the oxygen influence, Acta Materialia. 59 (2011) 5982–5988. https://doi.org/10.1016/j.actamat.2011.06.006.

[27] M.J. Lai, C.C. Tasan, D. Raabe, On the mechanism of {332} twinning in metastable β titanium alloys, Acta Materialia. 111 (2016) 173–186. https://doi.org/10.1016/j.actamat.2016.03.040.

[28] M.F. Ijaz, L. Héraud, P. Castany, I. Thibon, T. Gloriant, Superelastic behavior of biomedical metallic alloys, Metall Mater Trans A. 51 (2020) 3733–3741. https://doi.org/10.1007/s11661-020-05840-y.

[29] Z.W. Zhu, C.Y. Xiong, J. Wang, R.G. Li, Y. Ren, Y.D. Wang, Y. Li, In situ synchrotron X-ray diffraction investigations of the physical mechanism of ultra-low strain hardening in Ti–30Zr–10Nb alloy, Acta Materialia. 154 (2018) 45–55. https://doi.org/10.1016/j.actamat.2018.05.034.

[30] J.A. Klostermann, The concept of the habit plane and the phenomenological theories of the martensite transformation, Journal of the Less Common Metals. 28 (1972) 75–94. https://doi.org/10.1016/0022-5088(72)90170-1.

[31] T. Inamura, J.I. Kim, H.Y. Kim, H. Hosoda, K. Wakashima, S. Miyazaki, Composition dependent crystallography of α″-martensite in Ti–Nb-based β–titanium alloy, Philosophical Magazine. 87 (2007) 3325–3350. https://doi.org/10.1080/14786430601003874.

[32] E.G. Obbard, Y.L. Hao, R.J. Talling, S.J. Li, Y.W. Zhang, D. Dye, R. Yang, The effect of oxygen on α″ martensite and superelasticity in Ti–24Nb–4Zr–8Sn, Acta Materialia. 59 (2011) 112–125. https://doi.org/10.1016/j.actamat.2010.09.015.

[33] Y.W. Chai, H.Y. Kim, H. Hosoda, S. Miyazaki, Self-accommodation in Ti–Nb shape memory alloys, Acta Materialia. 57 (2009) 4054–4064. https://doi.org/10.1016/j.actamat.2009.04.051.

[34] E. Bertrand, P. Castany, Y. Yang, E. Menou, L. Couturier, T. Gloriant, Origin of {112}<111> antitwinning in a Ti–24Nb–4Zr–8Sn superelastic single crystal, Journal of Materials Science. 57 (2022) 7327–7342. https://doi.org/10.1007/s10853-022-07086-y.

[35] X. Zhang, W. Wang, J. Sun, Y. Gao, S.J. Pennycook, Enhanced twinning-induced plasticity effect by novel {315}α″/{332}β correlated deformation twins in a Ti–Nb alloy, International Journal of Plasticity. 148 (2022) 103132. https://doi.org/10.1016/j.ijplas.2021.103132.

[36] H. Tobe, H.Y. Kim, T. Inamura, H. Hosoda, T.H. Nam, S. Miyazaki, Effect of Nb content on deformation behavior and shape memory properties of Ti–Nb alloys, Journal of Alloys and Compounds. 577 (2013) S435–S438. https://doi.org/10.1016/j.jallcom.2012.02.023.

[37] M. Tahara, N. Okano, T. Inamura, H. Hosoda, Plastic deformation behaviour of single-crystalline martensite of Ti-Nb shape memory alloy, Sci Rep. 7 (2017) 15715. https://doi.org/10.1038/s41598-017-15877-6.

[38] D.H. Ping, Y. Yamabe-Mitarai, C.Y. Cui, F.X. Yin, M.A. Choudhry, Stress-induced α″ martensitic (110) twinning in β-Ti alloys, Appl. Phys. Lett. 93 (2008) 151911. https://doi.org/10.1063/1.3002295.

[39] M. Tahara, N. Otaki, D. Minami, T. Uesugi, Y. Takigawa, K. Higashi, T. Inamura, H. Hosoda, New dislocation dissociation accompanied by anti-phase shuffling in the α″ martensite phase of a Ti alloy, Acta Materialia. 227 (2022) 117705. https://doi.org/10.1016/j.actamat.2022.117705.

[40] D. De Fontaine, N.E. Paton, J.C. Williams, The omega phase transformation in titanium alloys as an example of displacement controlled reactions, Acta Metallurgica. 19 (1971) 1153–1162. https://doi.org/10.1016/0001-6160(71)90047-2.

[41] Y. Zheng, R.E.A. Williams, D. Wang, R. Shi, S. Nag, P. Kami, J.M. Sosa, R. Banerjee, Y. Wang, H.L. Fraser, Role of ω phase in the formation of extremely refined intragranular α precipitates in metastable β-titanium alloys, Acta Materialia. 103 (2016) 850–858. https://doi.org/10.1016/j.actamat.2015.11.020.

[42] A. Devaraj, S. Nag, R. Srinivasan, R.E.A. Williams, S. Banerjee, R. Banerjee, H.L. Fraser, Experimental evidence of concurrent compositional and structural instabilities leading to ω precipitation in titanium–molybdenum alloys, Acta Materialia. 60 (2012) 596–609. https://doi.org/10.1016/j.actamat.2011.10.008.

[43] A. Ramalohary, P. Castany, P. Laheurte, F. Prima, T. Gloriant, Superelastic property induced by low-temperature heating of a shape memory Ti–24Nb–0.5Si biomedical alloy, Scripta Materialia. 88 (2014) 25–28. https://doi.org/10.1016/j.scriptamat.2014.06.009.

[44] F. Sun, D. Laillé, T. Gloriant, Thermal analysis of the ω nanophase transformation from the metastable β Ti–12Mo alloy, J Therm Anal Calorim. 101 (2010) 81–88. https://doi.org/10.1007/s10973-010-0713-0.

[45] J. Dutta, G. Ananthakrishna, S. Banerjee, On the athermal nature of the β to ω transformation, Acta Materialia. 60 (2012) 556–564. https://doi.org/10.1016/j.actamat.2011.10.005.

[46] F. Sun, F. Prima, T. Gloriant, High-strength nanostructured Ti–12Mo alloy from ductile metastable beta state precursor, Materials Science and Engineering: A. 527 (2010) 4262–4269. https://doi.org/10.1016/j.msea.2010.03.044.

[47] R.I. Jaffee, The physical metallurgy of titanium alloys, Progress in Metal Physics. 7 (1958) 65–163. https://doi.org/10.1016/0502-8205(58)90004-2.

[48] H. Dammak, A. Dunlop, D. Lesueur, Study of the irradiation-induced α→ω phase transformation in titanium: Kinetics and mechanism, Philosophical Magazine A. 79 (1999) 147–166. https://doi.org/10.1080/01418619908214280.

[49] T.S. Kuan, R.R. Ahrens, S.L. Sass, The Stress-induced omega phase transformation in Ti-V alloys, MTA. 6 (1975) 1767–1774. https://doi.org/10.1007/BF02642306.

[50] M.J. Lai, C.C. Tasan, J. Zhang, B. Grabowski, L.F. Huang, D. Raabe, Origin of shear induced β to ω transition in Ti–Nb-based alloys, Acta Materialia. 92 (2015) 55–63. https://doi.org/10.1016/j.actamat.2015.03.040.

[51] S. Banerjee, P. Mukhopadhyay, Phase Transformations: Examples from Titanium and Zirconium Alloys, Elsevier, 2010.

[52] E. Sukedai, M. Shimoda, H. Nishizawa, Y. Nako, Nucleation Behaviour of β to ω Phase Transformations in β-Type Ti–Mo Alloys, Materials Transactions. 52 (2011) 324–330. https://doi.org/10.2320/matertrans.MB201017.

[53] S.Q. Wu, D.H. Ping, Y. Yamabe-Mitarai, W.L. Xiao, Y. Yang, Q.M. Hu, G.P. Li, R. Yang, {112}⟨111⟩ Twinning during ω to body-centered cubic transition, Acta Materialia. 62 (2014) 122–128. https://doi.org/10.1016/j.actamat.2013.09.040.

[54] J.W. Christian, S. Mahajan, Deformation twinning, Progress in Materials Science. 39 (1995) 1–157. https://doi.org/10.1016/0079-6425(94)00007-7.

[55] F. Niessen, A.A. Gazder, D.R.G. Mitchell, E.V. Pereloma, In-situ observation of nucleation, growth and interaction of deformation-induced α″ martensite in metastable Ti–10V–2Fe–3Al, Materials Science and Engineering: A. 802 (2021) 140237. https://doi.org/10.1016/j.msea.2020.140237.

[56] K. Cho, R. Morioka, S. Harjo, T. Kawasaki, H.Y. Yasuda, Study on formation mechanism of {332}<113> deformation twinning in metastable β-type Ti alloy focusing on stress-induced α″ martensite phase, Scripta Materialia. 177 (2020) 106–111. https://doi.org/10.1016/j.scriptamat.2019.10.011.

[57] B. Qian, L. Lilensten, J. Zhang, M. Yang, F. Sun, P. Vermaut, F. Prima, On the transformation pathways in TRIP/TWIP Ti–12Mo alloy, Materials Science and Engineering: A. 822 (2021) 141672. https://doi.org/10.1016/j.msea.2021.141672.

[58] B. Qian, M. Yang, L. Lilensten, P. Vermaut, F. Sun, F. Prima, In-situ observations of a hierarchical twinning–detwinning process in stress-induced α″-martensite of Ti–12Mo alloy, Materials Research Letters. 10 (2022) 45–51. https://doi.org/10.1080/21663831.2021.2013967.

[59] M.F. Ijaz, H.Y. Kim, H. Hosoda, S. Miyazaki, Superelastic properties of biomedical (Ti–Zr)–Mo–Sn alloys, Materials Science and Engineering: C. 48 (2015) 11–20. https://doi.org/10.1016/j.msec.2014.11.010.

[60] J. Fu, A. Yamamoto, H.Y. Kim, H. Hosoda, S. Miyazaki, Novel Ti-base superelastic alloys with large recovery strain and excellent biocompatibility, Acta Biomaterialia. 17 (2015) 56–67. https://doi.org/10.1016/j.actbio.2015.02.001.

[61] J. Zhang, F. Sun, Z. Chen, Y. Yang, B. Shen, J. Li, F. Prima, Strong and ductile beta Ti–18Zr–13Mo alloy with multimodal twinning, Materials Research Letters. 7 (2019) 251–257. https://doi.org/10.1080/21663831.2019.1595763.

[62] M.F. Ijaz, D. Laillé, L. Héraud, D.-M. Gordin, P. Castany, T. Gloriant, Design of a novel superelastic Ti–23Hf–3Mo–4Sn biomedical alloy combining low modulus, high strength and large recovery strain, Materials Letters. 177 (2016) 39–41. https://doi.org/10.1016/j.matlet.2016.04.184.

[63] L. Lilensten, J.-P. Couzinié, J. Bourgon, L. Perrière, G. Dirras, F. Prima, I. Guillot, Design and tensile properties of a bcc Ti-rich high-entropy alloy with transformation-induced plasticity, Materials Research Letters. 5 (2017) 110–116. https://doi.org/10.1080/21663831.2016.1221861.

[64] J.J. Gao, P. Castany, T. Gloriant, Synthesis and characterization of a new TiZrHfNbTaSn high-entropy alloy exhibiting superelastic behavior, Scripta Materialia. 198 (2021) 113824. https://doi.org/10.1016/j.scriptamat.2021.113824.

[65] Y. Yang, P. Castany, M. Cornen, I. Thibon, F. Prima, T. Gloriant, Texture investigation of the superelastic Ti–24Nb–4Zr–8Sn alloy, Journal of Alloys and Compounds. 591 (2014) 85–90. https://doi.org/10.1016/j.jallcom.2013.12.207.

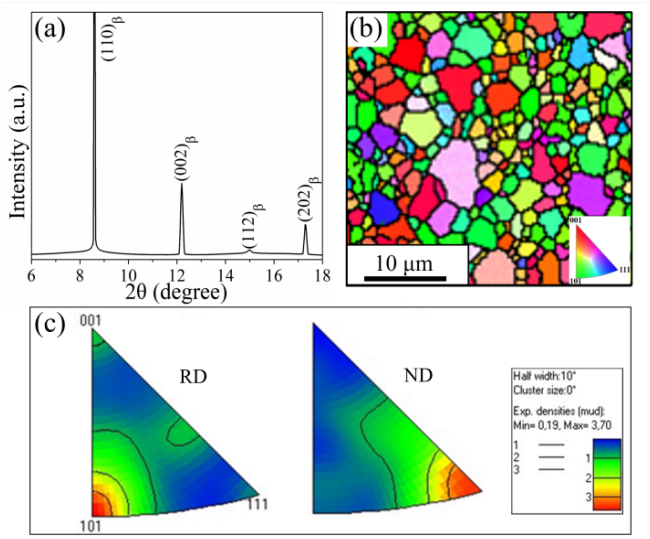

Fig.1 Initial microstructure of the short solution treatment Ti2033 sample: SXRD profile acquired before deformation (a); EBSD IPF map along RD (rolling direction) (b) and corresponding IPF (c).

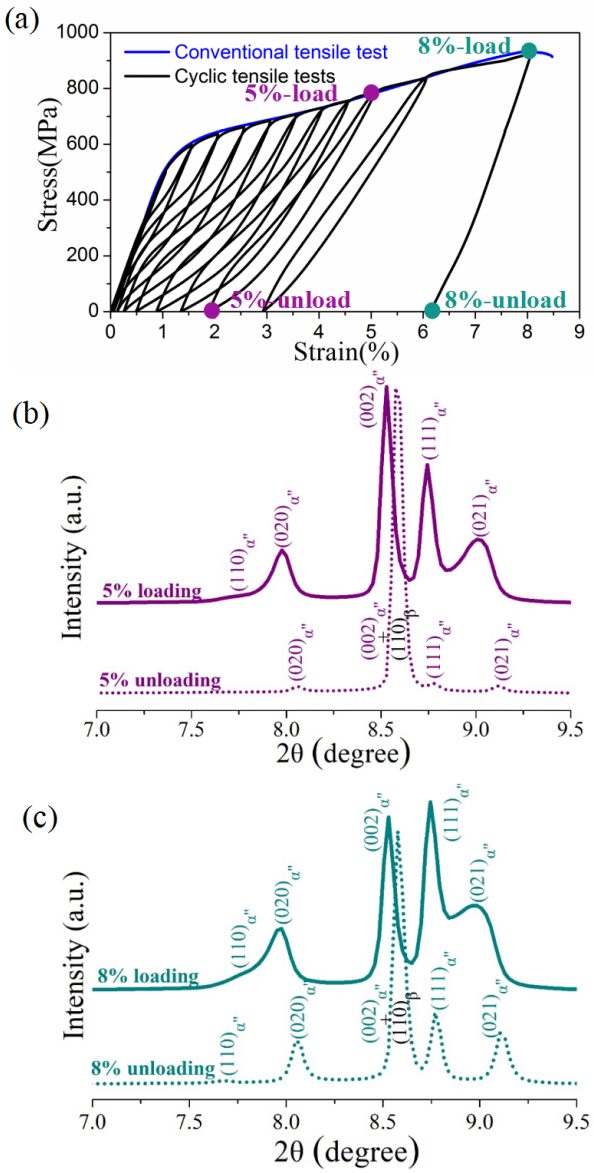

Fig.2 Conventional and cyclic engineering tensile curves with the two deformed samples at 5% and 8% of strain (a); corresponding SXRD profiles acquired under loading (solid lines) and after unloading (dashed lines) from 5% (b) and 8% (c) of strain.

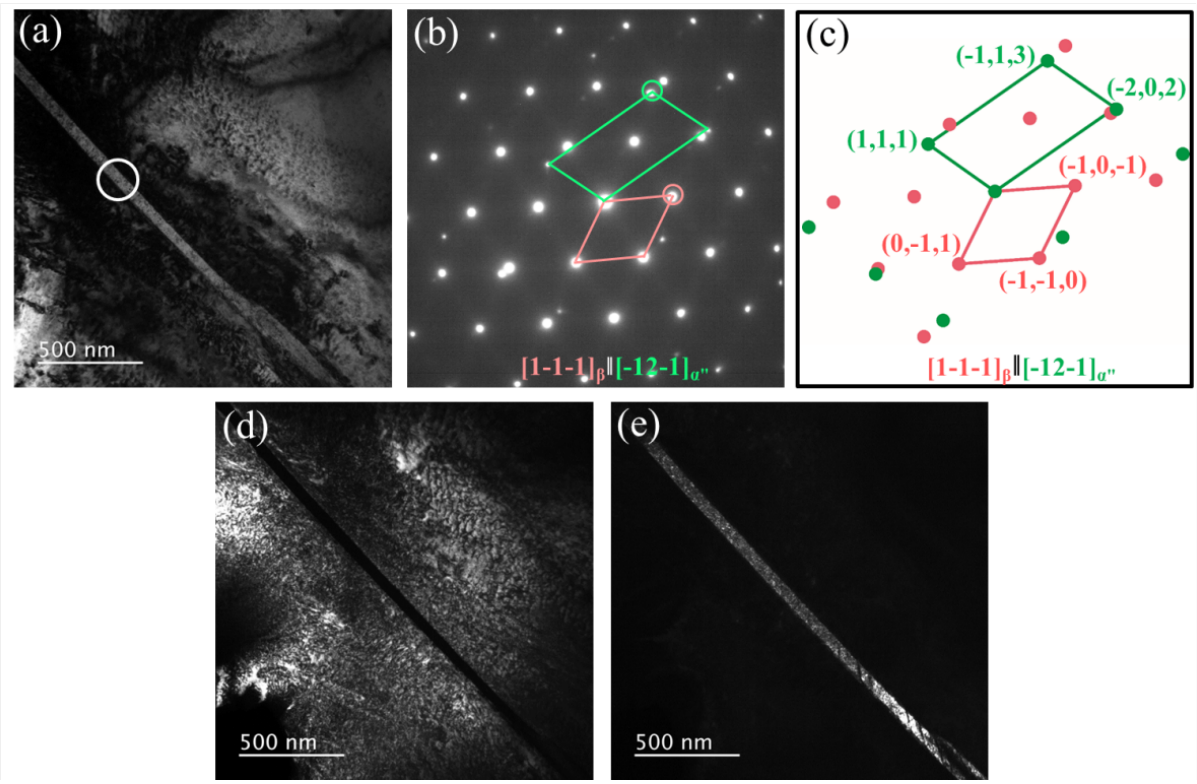

Fig.3 TEM observation of the deformed sample at 5% of strain: bright-field image with a single deformation band (a); corresponding SAED pattern of the white circle area (b), and its indexed key diagram (c); dark-field images taken with the spots encircled in red (d) and green (e) in the SAED pattern.

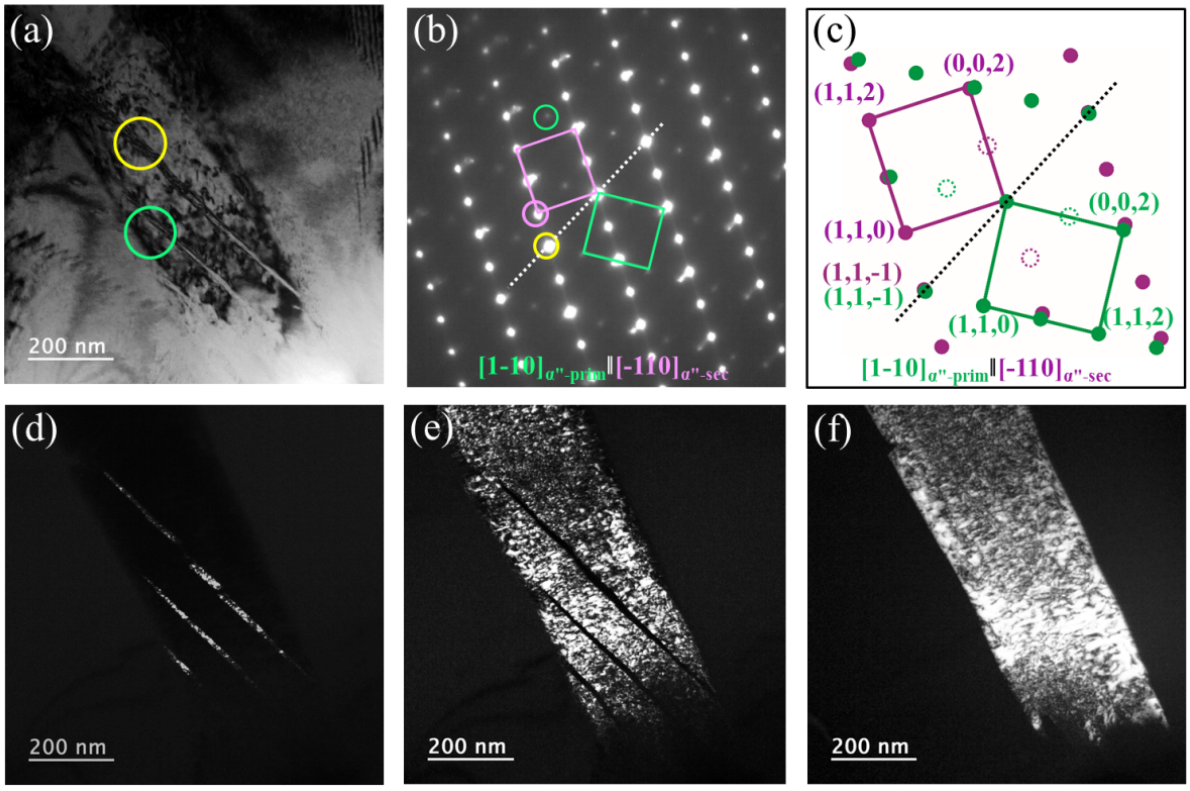

Fig.4 TEM observation of the deformed sample at 8% of strain: typical bright-field image of deformation microstructure with hierarchical bands (a); corresponding SAED pattern in the yellow circle (b), and its key diagram (c); dark-field images taken with the spots encircled in green (d), purple (e), and yellow (f) in the SAED pattern.

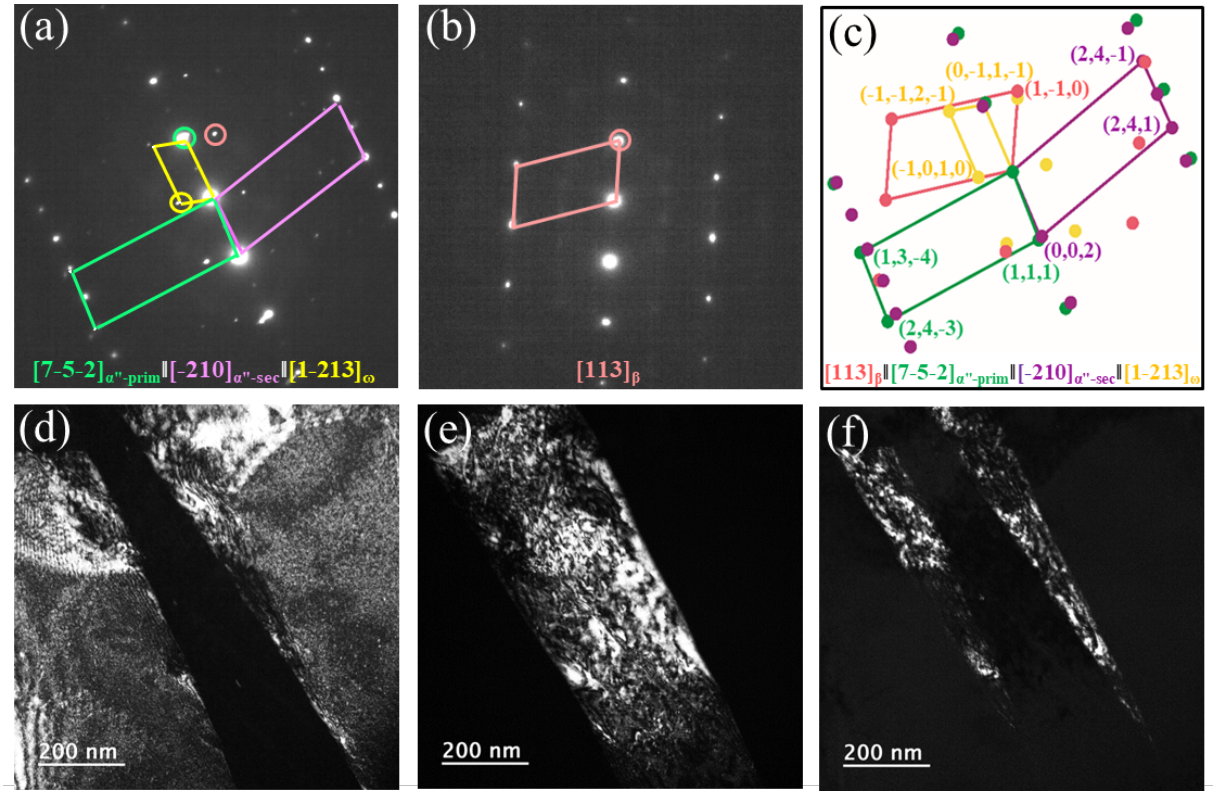

Fig.5 TEM observation of the deformed sample at 8% of strain for a different diffraction condition: SAED pattern corresponding to the area encircled in green in Fig.4a (a); SAED pattern of the β matrix only (b); key diagram for SAED patterns (c); dark-field images taken with the spots encircled in red (d), green (e) and yellow (f) in the SAED patterns.

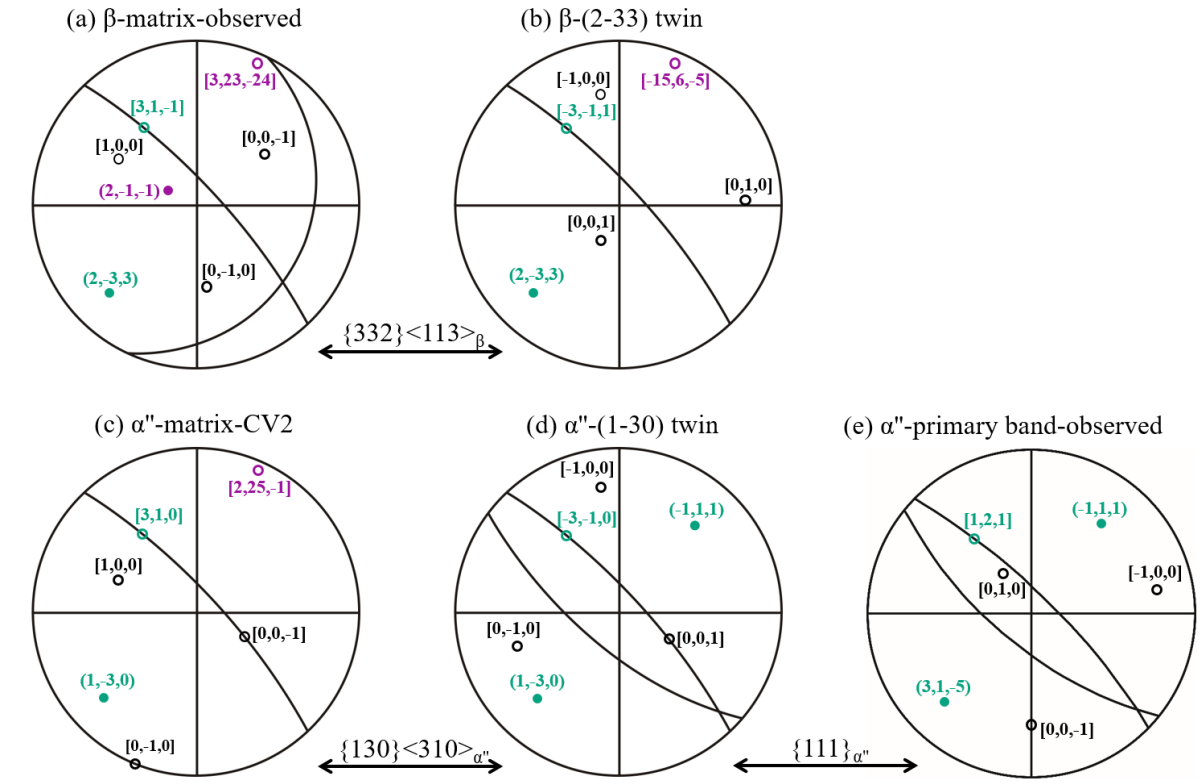

Fig.6 Stereographic projections for the sample deformed at 5%: observed β matrix in Fig.3 (a); deduced (2-33)[31-1]$_{\beta}$ twin (b); reconstructed α″ martensitic variant (c); deduced (1-30)$_{\alpha''}$ twin (d); observed α″ band in Fig.3 (e).

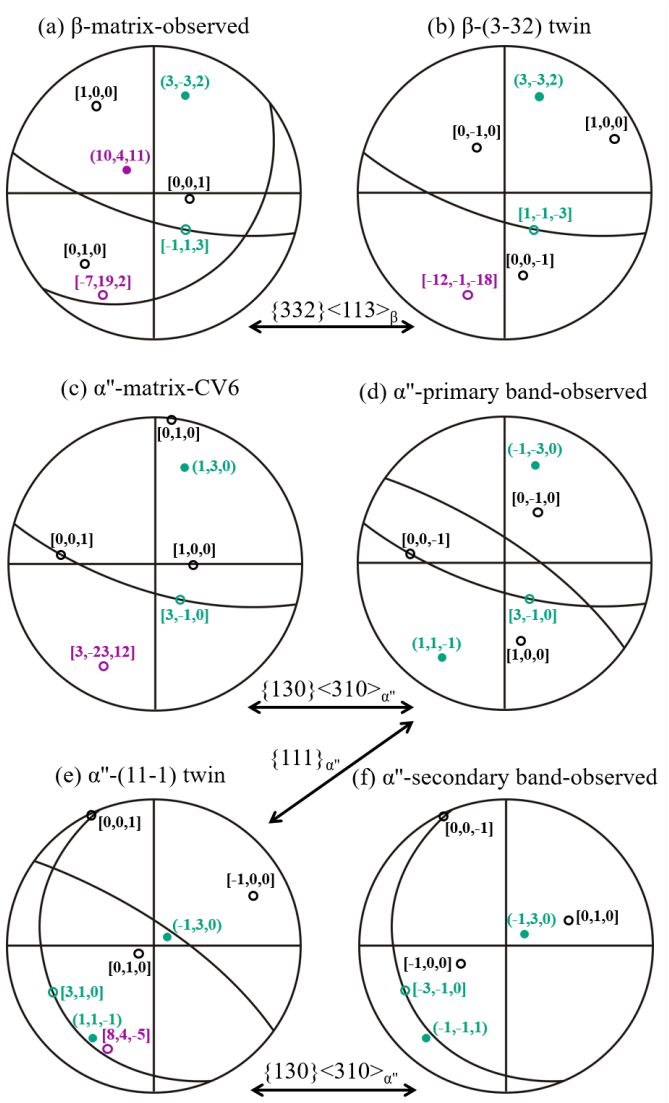

Fig.7 Stereographic projections for the sample deformed at 8%: observed β matrix in Fig.4-5 (a); deduced (3-32)[-113]$_{\beta}$ twin (b); reconstructed α″ martensitic variant (c); observed α″ primary band in Fig.4-5 (d); deduced (11-1)$_{\alpha''}$ twin (e); observed α″ secondary band in Fig.4-5 (f).

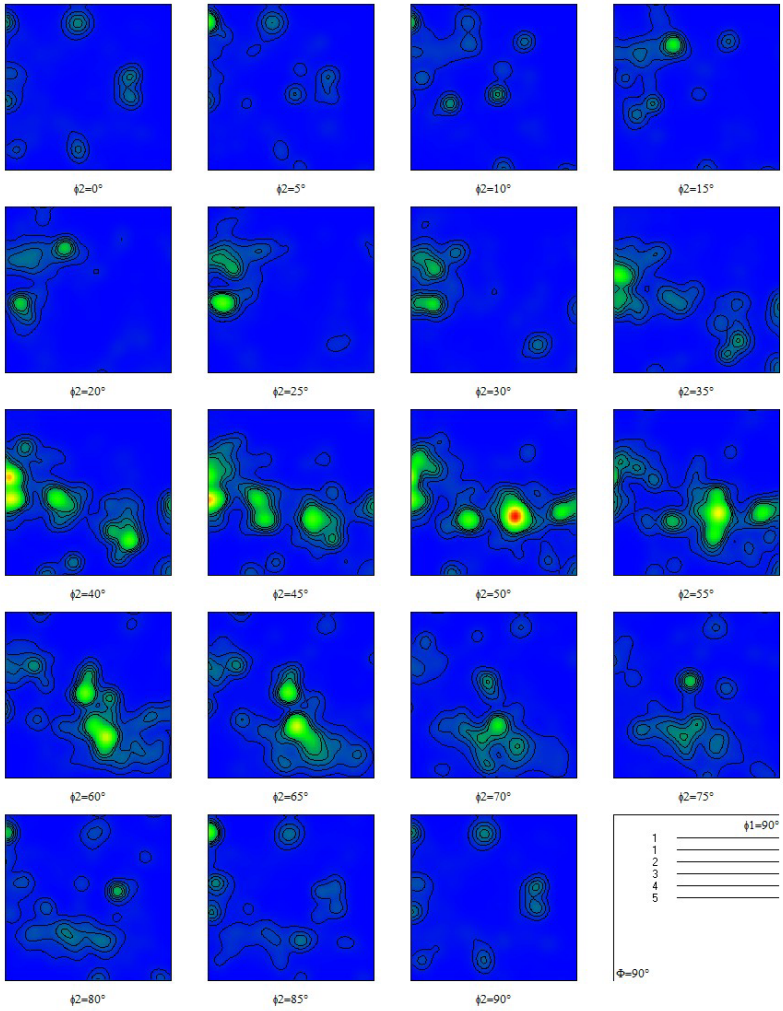

Fig.S1 Orientation distribution function (ODF) of the heat-treated Ti2033 sample.

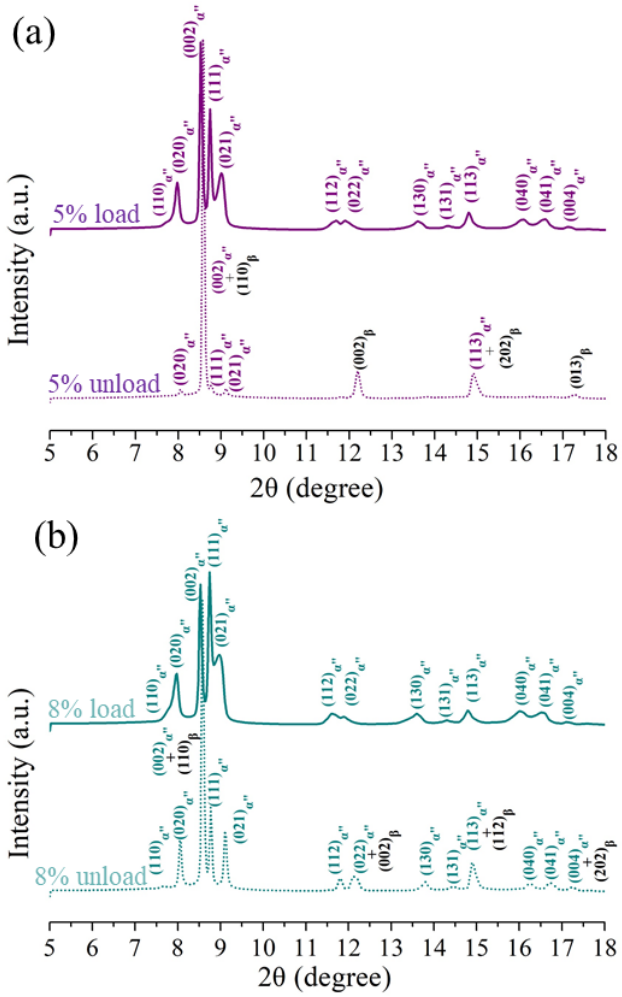

Fig.S2 Entire SXRD profiles acquired under loading (solid line) and after unloading (dashed line) at 5% (a) and 8% (b) of strain.

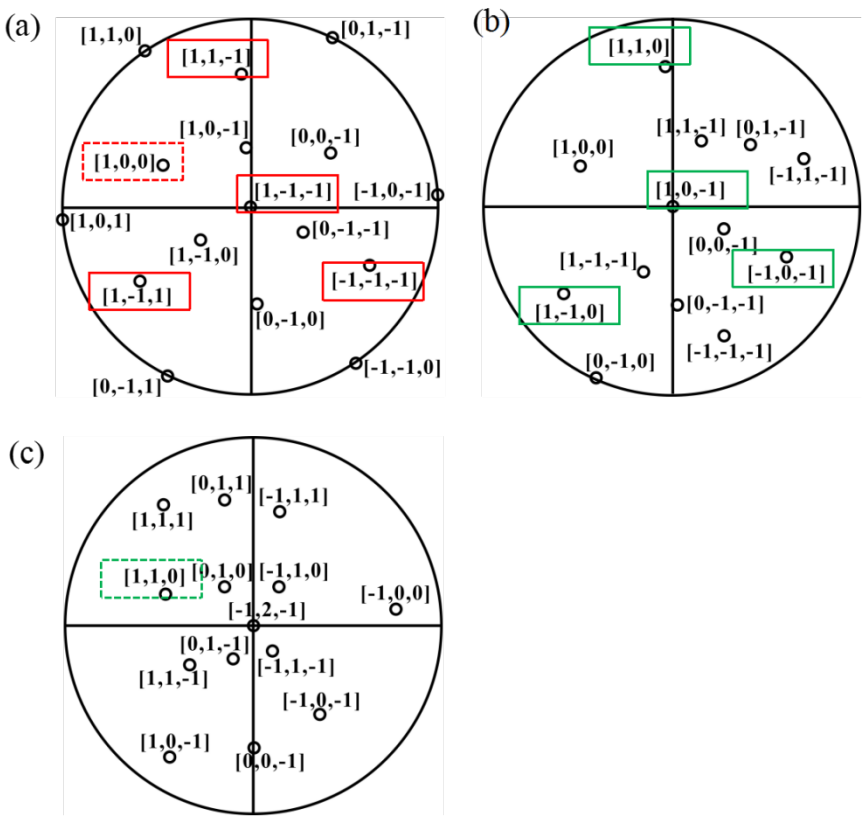

Fig.S3 Stereographic projections of the observed β phase (a) and SIM α" phase with the classical OR (b); comparison with the stereographic projection of the observed α″ band in Fig.3e (c) for the 5% strained specimen.

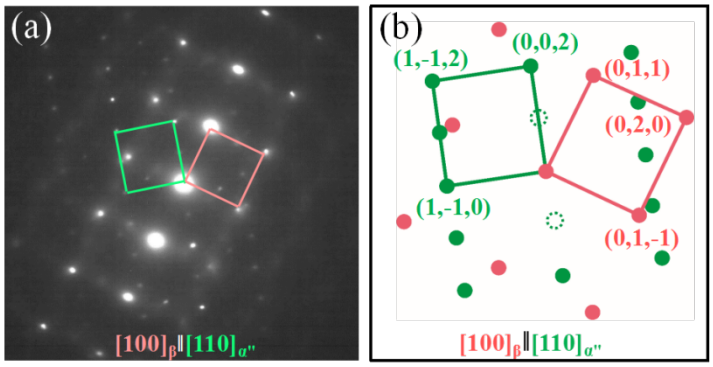

Fig.S4 Another diffracting condition of the specimen strained to 5% : SAED pattern of the white circled area in Fig.3a (a), and its indexed key diagram (b). Both zone axes are not exactly parallel due to the orientation relationship between twin and matrix and are indicated by dashed lines in the Fig.S3.